DOI: 10.19884/j.1672-5220.202404014

Architecture of Necklace-Like Carbon Nanotubes @ Silicon Oxycarbide Nanostructure for Stable Lithium Storage

GAZI Farhan Ishraque Toki, RANA Zafar Abbas Manj, MA Yuanyuan*, YANG Jianping*
State Key Laboratory of Advanced Fiber Materials, College of Materials Science and Engineering, Donghua University, Shanghai 201620, China

Abstract: Silicon oxycarbide (SiOC) has emerged as a promising candidate for anode materials in lithium-ion batteries (LIBs) due to its unique properties. However, the low electrical conductivity of SiOC limits its practical applications. Herein, a novel necklace-like nanostructure was fabricated through the sol-gel method by embedding SiOC nanospheres in carbon nanotubes (CNTs) to form a stable electronic pathway within the structure. Controlling the hexadecyl trimethyl ammonium bromide (CTAB) content through CTAB removal and centrifugation to separate SiOC and CNTs @ phenylene-bridged mesoporous organosilica (CNTs @ PBMO) before the calcination is important to achieve the necklace-like CNTs @ SiOC nanostructure. The fabricated porous necklace-like CNTs@SiOC nanostructure not only improved the electrical conductivity but also ensured full utilization of SiOC active sites during discharging/charging along with accelerating ion penetration. As a result, it provided a remarkably long cycling life of up to 1 400 cycles, retaining a specific capacity of 178 mA·h/g.

Keywords: necklace-like structure; CNTs @ SiOC; sol-gel method; long cycle; lithium-ion battery (LIB)
CLC number: TQ152 **Document code**: A
Article ID: 1672-5220(2026)02-0032-11

Open Science Identity (OSID)

0 Introduction

Since the beginning of the 21st century, lithium-ion batteries (LIBs) have been crucial for us to move from internal combustion engine-based mobility to electric automobiles[1]. LIBs are preferred over other batteries, such as nickel-based and lead-acid batteries, to meet the growing demand for energy storage devices due to their high energy and power density. However, commercially available LIBs are far from meeting the demand for electric vehicles because they are based on carbon anode materials with a low theoretical specific capacity of 372 mA·h/g[2]. Silicon (Si) is considered as an alternative anode material due to its high theoretical specific capacity (4 200 mA·h/g) and low discharge plateau (0.4 V). However, its application is hindered by the significant volume expansion (300%) during discharging/charging[3]. The increased volumetric strain leads to polarization of the Si-based anode and lowers its electrical conductivity, ultimately leading to capacity loss[4-5]. Currently, some strategies, including nanostructuring or embedding Si particles in various matrices, have gained attention to overcome this limitation[6-7].

In contrast, silicon oxycarbide (SiOC) exhibits superior structural stability over crystalline Si because of its low volume expansion rate of 22% and the advantages of simple composition and suitability for mass production[8-9]. In comparison to crystalline Si, SiOC is suitable for an anode material[10]. Among several techniques, the polymer-derived ceramic (PDC) method is efficient for synthesizing SiOC. In this method, a suitable polymeric precursor undergoes controlled pyrolysis in a specific environment, yielding the desired ceramic material. The PDC method offers superior control over the ceramic composition compared to alternative processing methods like sol-gel processing[11]. The ceramics that have undergone pyrolysis are usually amorphous, lacking a distinct crystalline structure. SiOC has tetrahedral structural units consisting of $SiO_{4-x}C_x$, enabling it to accommodate volume variations during discharging/charging. The amount of disordered carbon produced by pyrolysis of polymeric precursors varies. The micro-mesoporous structure facilitates lithium-ion (Li-ion) insertion and mitigates volume fluctuations[12-14]. However, in practice, the insufficient conductivity of SiOC due to disordered carbon limits the rate performance at high current densities.

Over the years, several doping materials have been utilized to enhance the performance of SiOC as the anode in LIBs[15-17]. Among those, carbon possessing excellent electrical conductivity can significantly improve the conductivity of SiOC, thus improving the material's specific capacity and rate performance[18-19]. Carbon nanotubes (CNTs)[20], graphite[21], or graphene[22] have

Received date: 2024-04-29
Foundation items: National Natural Science Foundation of China (Nos. 92163121 and 52122312)
* Correspondence should be addressed to MA Yuanyuan, email: yyma@dhu.edu.cn; YANG Jianping, email: jianpingyang@dhu.edu.cn
Citation: GAZI F I T, RANA Z A M, MA Y Y, et al. Architecture of necklace-like carbon nanotubes@silicon oxycarbide nanostructure for stable lithium storage [J]. *Journal of Donghua University (English Edition)*, 2026, 43(2): 32-42.

been incorporated into SiOC. For example, SiOC nanolayer-implanted graphite anodes retained 80% of the initial capacity due to the high electrical conductivity and structural stability of graphite[21]. A composite of SiOC and nitrogen-doped graphene aerogel exhibited high cycling stability up to 1 000 cycles because of the high conductivity of graphene aerogel and the enhanced free carbon content on SiOC[23]. Boron doping reduced the interparticle resistance of the B-SiOC@G anode, whereas graphene ensured high electrical conductivity and secured structual stability up to 1 000 cycles[22]. In contrast, the SiOC-CNT structure made from pyrolysis of CNTs in 1,3,5,7-tetramethyl-1,3,5,7-tetravinyl cyclotetrasiloxane (TTCS) exhibited a specific capacity retention of 81.5% after only 40 cycles even though CNTs were introduced to enhance the electrical conductivity[20]. Recently, a unique necklace-designed SiO_x-based anode substantial incorporating CNTs supported SiO_x/C@C spheres with a surface carbon coating layer showed high cycling stability up to 1 000 cycles[24]. In the study, the CNT networks mitigated volume expansion and stabilized the formation of the solid electrolyte interphase (SEI) through the necklace-like structure. To date, no such necklace-like structure has been reported for SiOC-based nanospheres onto CNTs to evaluate the performance as anode materials.

Herein, necklace-like CNTs@SiOC are fabricated by the sol-gel method. The formation of a necklace-like CNTs@SiOC structure would be achieved by taking advantage of the self-assembly of hemimicelles around the hydrophobic surface of CNTs. CNTs would form stable conductive pathways throughout the structure, and be an excellent active material as an anode material for LIBs. The directed assembly of necklace-like CNTs@SiOC on the CNT surface could efficiently reduce the interparticle resistance of SiOC, and the incorporation of CNTs could further preserve the structural integrity and enhance the electrical conductivity during discharging/charging. Furthermore, the porosity of the necklace-like CNTs@SiOC structure would shorten the diffusion distance for Li ions. On the whole, such novel CNTs@SiOC structure would enhance the conductivity, employ the active sites of SiOC, and ensure efficient Li-ion diffusion via the porous network during discharging/charging.

1 Materials and Methods

1.1 Materials

Ethanol, hexadecyl trimethyl ammonium bromide (CTAB), aqueous ammonia (NH_4OH), 1, 4-bis (triethoxysilyl) benzene (BTEB), and CNTs were purchased from Xilong (China), Sigma-Aldrich (USA), Sigma-Aldrich (USA), Leyan (China), and Shanghai New Carbon Materials Company (China), respectively. Ethylene carbonate (EC), ethyl methyl carbonate (EMC), and dimethyl carbonate (DMC) were purchased from Capchem Technology Co. Ltd., China. All the purchased materials were utilized as received without further purification.

1.2 Preparation of CNTs @ phenylene-bridged mesoporous organosilica (CNTs @ PBMO) nanospheres

The CNTs @ PBMO nanospheres were initially formed by the Stöber method. For a standard synthesis, a mixture of 120 mL ethanol and 280 mL deionized water was added into the three-necked round-bottom flask. Then, 10 mg CNTs were evenly dispersed into the mixed ethanol/water solution via ultrasonication for 2 h. After that, 800 mg CTAB was evenly dissolved into the above dispersion. Subsequently, 4 mL NH_4OH solution with a volume fraction of 25% was added under continuous stirring. After stirring for 1 h, 1 mL BTEB was gradually added to the dispersion with continuous stirring for 16 h. The solid particles were retrieved from the aforementioned dispersion via centrifugation and subsequent washing with water and ethanol. The as-collected CNTs @ PBMO nanospheres were dried in a vacuum oven overnight at 60 ℃.

1.3 Preparation of necklace-like CNTs @ SiOC nanospheres

The collected dried CNTs@PBMO nanospheres were further processed to prepare necklace-like CNTs@SiOC nanospheres through CTAB extraction. First, CNTs@PBMO nanospheres were dispersed in a 60 mL ethanol solution containing 6 mL HCl (a volume fraction of 37%). CTAB was successfully removed while stirring at 60 ℃ for 24 h. Further, the heavy-weighted CNTs @ PBMO nanospheres were separated from the single-formed SiOC nanospheres by centrifugation at 5 000 r/min. Subsequently, the resultant product was washed with deionized water under three times ultrasonication and vacuum-dried at 60 ℃. The solid CNTs @ PBMO nanospheres were further calcined at a temperature of 800 ℃ in an argon atmosphere for 10 h, and a heating rate of 2 ℃/min to form necklace-like CNTs@SiOC nanospheres. In addition, CNTs @ SiOC-5 and CNTs@SiOC-15 nanospheres were prepared similarly but without centrifugation, in which 5 and 15 denoted the CNT masses of 5 mg and 15 mg, respectively.

For comparison, SiOC nanospheres were prepared through the formation of PBMO nanospheres by the Stöber method. For a standard synthesis, 1 600 mg CTAB was distributed in a solution consisting of 240 mL ethanol and 560 mL deionized water. Subsequently, 8 mL NH_4OH was added. After continuous stirring for 1 h, 1 mL BTEB was added gradually and stirred continuously for an additional 14 h at a moderate stirring rate. Monodisperse PBMO nanospheres were obtained after centrifugation and drying. The samples were washed three times through centrifugation by using deionized water and ethanol. The PBMO nanospheres, as they were originally synthesized, underwent a heating process in an argon environment at a temperature of 800 ℃ for 10 h and a ramping rate of 2 ℃, and SiOC

nanospheres were successfully formed.

1.4 Material characterization

1.4.1 Scanning electron microscopy (SEM) analysis

Field emission scanning electron microscopy (FESEM) captures the images of the samples Hitachi SU8010 (Hitachi, Japan) FESEM instrument.

1.4.2 Transmission electron microscopy (TEM) analysis

TEM observations were performed by employing a JEM-2100 F microscope (JEOL, Japan) operating at 200 kV. While field emission transmission electron microscopy (FETEM) was performed by employing a Talos F200 S microscope (Thermo Fisher Scientific Inc., Czech) at 200 kV.

1.4.3 X-ray diffraction (XRD) analysis

XRD patterns were obtained by employing a Rigaku D/Max-2550 PC diffractometer (Tokyo, Japan) in a 2θ range of 10° to 90°.

1.4.4 Fourier transform infrared (FTIR) spectroscopy test

The FTIR analysis was conducted by employing a Nicolet-NEXUS 670 spectrophotometer (Thermo Nicolet, USA).

1.4.5 Raman spectrum analysis

The Raman spectra were acquired by using a Dilor LabRam-1B microscopic Raman spectrometer (HORIBA Scientific, Japan). The excitation was performed by the Raman instrument with a He-Ne laser at a wavelength of 532 nm.

1.4.6 Thermalgravimetric analysis (TGA)

TGA was conducted by employing a TG 209F1 apparatus (NETZSCH-Gerätebau GmbH, Germany) in an air atmosphere. The assessment was performed across a temperature range of 50 to 800 ℃, with a heating rate of 10 ℃/min.

1.4.7 Brunauer-Emmett-Teller (BET) and Barrett-Joyner-Halenda (BJH) analysis

The Autosorb-iQ machine (Anton Paar, Austria) was used to measure nitrogen sorption isotherms. Prior to measurement, the samples underwent degassing under vacuum at a temperature of 180 ℃ for at least 10 h. The specific surface areas were calculated by using the BET method, based on the adsorption data obtained at P/P_0 of 0.02–0.20, where P denotes the equilibrium pressure and P_0 denotes the saturation pressure. The pore size distribution was determined by using the BJH model for the adsorption branch.

1.4.8 X-ray photoelectron spectroscopy (XPS) analysis

The Escalab 250Xi spectrometer (Thermo Fisher Scientific Inc., USA) was used to conduct XPS analysis in order to determine the valence state of various elements in necklace-like nanostructures.

1.5 Electrochemical measurement

The working anode was fabricated by mixing active materials, carbon black and sodium alginate at a mass ratio of 70∶15∶15 in deionized water. The slurry was evenly applied onto copper (Cu) foil and subjected to vacuum drying at a temperature of 70 ℃ for 12 h to remove deionized water. The active substance was loaded with a quantity of 0.6–1.0 mg/cm^2. The CR2032 coin-type half cells were assembled in an argon-filled glove box with a minimum of water and oxygen (less than 0.1 parts per million). The cathode was made of Li foil. The electrolyte consisted of 1.0 mol/L $LiPF_6$ dissolved in a mixture of EC, EMC and DMC at a volume ratio of 3∶4∶3. Additionally, the electrolyte contained fluoroethylene carbonate additive with a mass fraction of 5%.

Galvanostatic charge/discharge (GCD) cycling tests were conducted on a Neware battery testing system (Neware, China) at different current densities within a voltage range of 0.01 to 2.00 V. Cyclic voltammetry (CV) experiments were performed by using a VMP3 electrochemical workstation. The CV scan rate was 0.1 mV/s within a voltage range of 0.01 to 2.00 V.

2 Results and Discussion

2.1 Fabrication and identification of necklace-like CNTs@SiOC nanospheres

The necklace-like CNTs @ SiOC nanospheres were fabricated through a self-growth assembly by the Stöber method, where the SiOC nanospheres were grown around CNTs (Fig. 1).

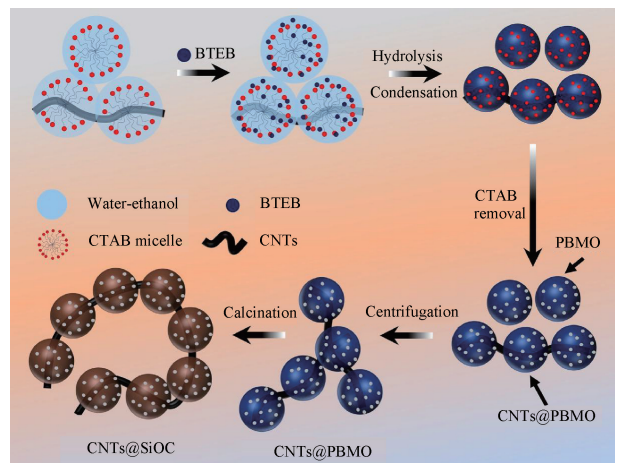

Fig. 1 Schematic diagram of necklace-like CNTs @ SiOC nanosphere fabrication

The cationic surfactant CTAB played a key role in the formation of the necklace-like CNTs @ SiOC nanospheres by forming hemimicelles around the CNTs[25]. The hydrophobic tail of CTAB and the surface of CNTs facilitated aggregation by the electrostatic force of attraction[26-27]. Meanwhile, the surfactant formed hemimicelles around the CNT surface due to the repulsion of cationic sides of CTAB in the water/ethanol solution[28-29]. Besides the hemimicelles on CNTs, some micelles were also formed in the solution. These

hemimicelles and micelles held the ethanol-phase inside and the water-phase outside due to differences in the dielectric constant and hydrophobic and hydrophilic sides of the surfactant. Due to their hydrophobic nature, BTEB diffused into the interior of hemimicelles and micelles, and initiated the growth of PBMO nanospheres around CNTs through hydrolysis and condensation catalyzed by ammonia[30].

The SiOC and necklace-like CNTs @ SiOC nanospheres were obtained by calcination after the removal of CTAB through centrifugation, as shown in the TEM image in Fig. 2(a). Further, to collect the pure necklace-like structure, the heavy-weighted necklace-like CNTs@PBMO nanospheres were separated from the single-formed PBMO nanospheres by centrifugation after removal of CTAB, and subsequently calcined to obtain the final necklace-like CNTs@SiOC nanospheres. TEM and SEM images clearly indicate the successful formation of necklace-like CNTs @ SiOC nanospheres as shown in Figs. 2(b) and 2(c), respectively. This stable conductive connection between SiOC nanospheres formed by CNTs can be useful to achieve long cycle life when being used in LIBs. The silicon is uniformly distributed in the prepared necklace-like CNTs@SiOC nanospheres, which is confirmed by the elemental mapping in Fig. 2(d).

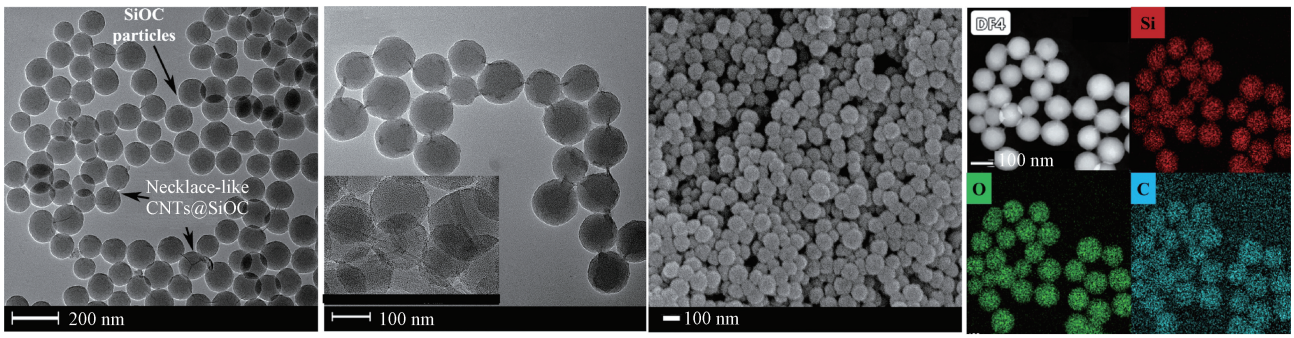

Fig. 2 Morphology results: (a) TEM image of combined SiOC and necklace-like CNTs@SiOC nanospheres; (b) TEM image of necklace-like CNTs@SiOC nanospheres with enlarged view in inset; (c) SEM image of necklace-like CNTs@SiOC nanospheres; (d) elemental mapping of necklace-like CNTs@SiOC nanospheres with dark-field probe (DF4)

The irregular SiOC and CNTs@SiOC-5 nanospheres are shown in Fig. 3(a). The aggregated CNTs@SiOC-15 nanospheres far from a necklace-like structure are shown in Fig. 3(b). The variation in the CNT mass directly disturbs the formation of CTAB hemimicelles around the CNTs at a certain volume ratio of water and ethanol, preventing the formation of a necklace-like nanostructure as reported in Ref. [31].

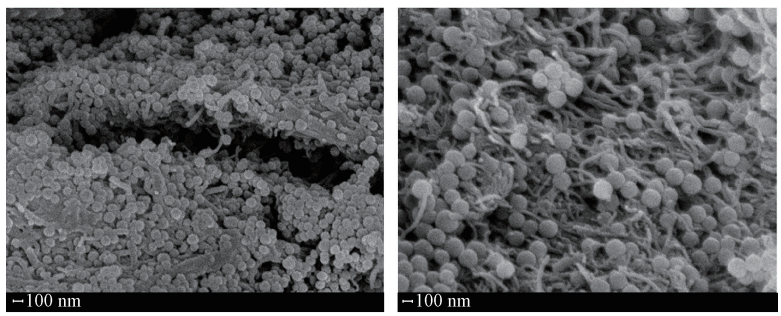

Fig. 3 SEM images of irregular nanospheres: (a) CNTs@SiOC-5; (b) CNTs@SiOC-15

2.2 Chemical characterization of CNTs@SiOC

Figure 4(a) shows the XRD patterns of SiOC and CNTs@SiOC. A prominent broad peak is observed at around 22°, indicating the presence of amorphous SiO_x and carbon in the SiOC nanospheres. Additionally, the shifted peak at 29° is detected for necklace-like CNTs@SiOC which is most likely due to the presence of sp^2 hybridized CNTs[24]. Similarly, the peak shifts from 22° for CNTs@SiOC-5 to 29° for CNTs @ SiOC-15 as reported in Ref. [32].

In Fig. 4(b), the FTIR peak observed at 1 376 cm^{-1} is identified as the presence of Si—O—C bonds, while the peak at 1 140 cm^{-1} is associated with Si—O and O—C bonds[22], indicating the successful incorporation of SiOC on the surface of CNTs. Peaks at 1 460 and 1 634 cm^{-1} indicate Si—CH_3 bonds, and peaks at 2 928 and 1 088 cm^{-1} indicate the presence of C—H bonds and Si—O bonds[33], respectively. The FTIR peaks indicate almost the same composition of CNTs @ SiOC-5 and CNTs@SiOC-15 as reported in Ref. [34].

Raman characterization was carried out to reveal the carbonization degree of SiOC and CNTs @ SiOC. In Fig. 4(c), two broad peaks at 1 316 and 1 586 cm^{-1} correspond to the D-band and G-band, respectively, as reported in Ref. [35]. The peak intensity ratios of the D-band to G-band (I_D/I_G) of SiOC and necklace-like CNTs@SiOC are 0.83 and 0.84, respectively, which indicates a high degree of carbonization. Similarly, CNTs@SiOC-5 and CNTs@SiOC-15 exhibit the same I_D/I_G of 0.83.

Figure 4(d) shows the thermogravimetric (TG) curves of SiOC and CNTs@SiOC in air. The mass loss rate of SiOC is about 9.2% which is probably due to the presence of amorphous carbon in the SiOC nanospheres. The mass loss rate of the carbon from necklace-like CNTs@SiOC is about 38.5%, indicating the content of CNTs in the structure[24]. The presence of CNTs in the unique structure would obviously play a role in maintaining an electrical pathway that contributes to enhancing the electrochemical performance. In addition, the mass loss rates of CNTs@SiOC-5 and CNTs@SiOC-15 are about 37.0% and 39.0%, respectively.

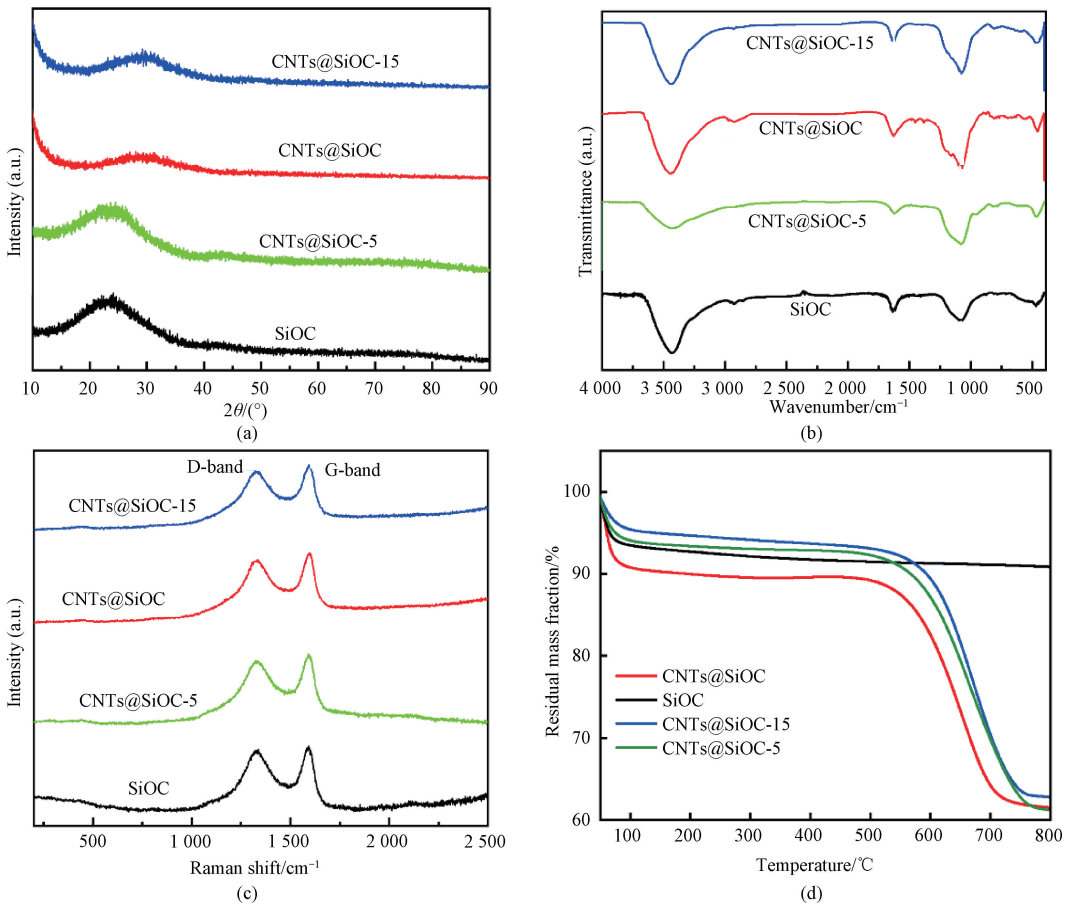

Fig. 4 Chemical characterization of necklace-like CNTs@SiOC, SiOC, CNTs@SiOC-5 and CNTs@SiOC-15: (a) XRD patterns; (b) FTIR spectra; (c) Raman spectra; (d) TG curves

Figure 5(a) presents the N_2 adsorption/desorption isotherms of SiOC and necklace-like CNTs@SiOC. BET N_2 adsorption measurement shows specific surface areas of 592.482 and 384.171 m^2/g for SiOC and necklace-like CNTs@SiOC, respectively, and the specific surface area of SiOC is higher than that of necklace-like CNTs@SiOC. Because of the integration of CNTs into SiOC, the specific surface area of necklace-like CNTs@SiOC is reduced. The average pore size of SiOC is 4.46 nm; in contrast, the average pore size of necklace-like CNTs@SiOC is slightly larger at 6.89 nm. This is because necklace-like CNTs@SiOC are formed after CTAB removal from CNTs@PBMO followed by calcination, and the available CTAB is not removed from PBMO nanospheres before calcination during the synthesis of SiOC. The larger pore size in the necklace-like CNTs@SiOC could facilitate the diffusion of Li ions by providing shorter Li-ion transport pathways.

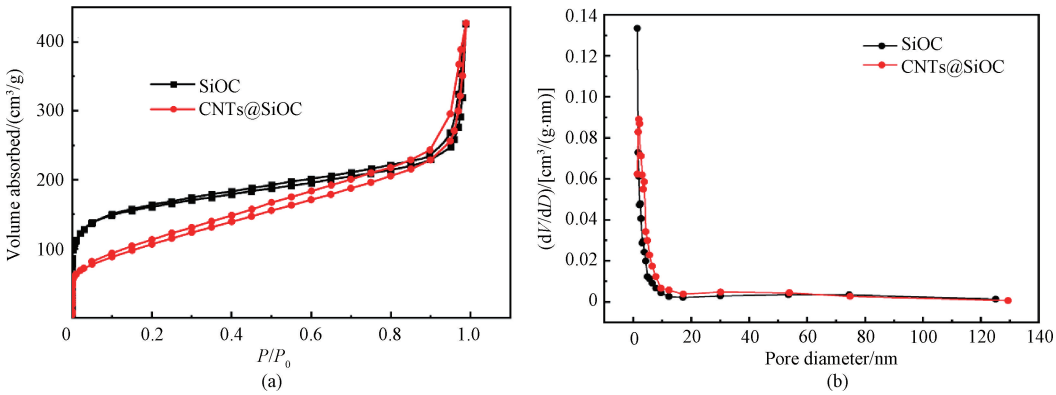

Fig. 5 Porosity of SiOC and necklace-like CNTs@SiOC: (a) N_2 adsorption/desorption isotherms; (b) pore diameter distribution with V and D denoting pore volume and pore diameter, respectively

High-resolution XPS measurements were performed to further investigate the chemical composition at the surface of necklace-like CNTs @ SiOC. The XPS spectrum of necklace-like CNTs@SiOC indicates the existence of Si, O and C elements as shown in Fig. 6(a). Additionally, the Si 2p spectrum (Fig. 6(b)) exhibits two peaks at 103.71 and 104.45 eV for the Si—O and Si—C bonds[36], respectively, indicating the existence of SiO_x and carbon. In particular, the O 1s spectrum (Fig. 6(c)) displays a distinct peak at 533.02 eV, corresponding to the Si—O bond. The C 1s spectrum (Fig. 6(d)) shows both C═C/C—C peak at 285.02 eV and C—O peak at 286.06 eV, respectively, suggesting the presence of a carbon network as reported in Ref. [24]. Overall, the peak intensity of oxygen is higher than that of carbon (Fig. 6(a)), thus clearly demonstrating that CNTs might be covered with SiOC on their surface as reported in Refs. [24, 37].

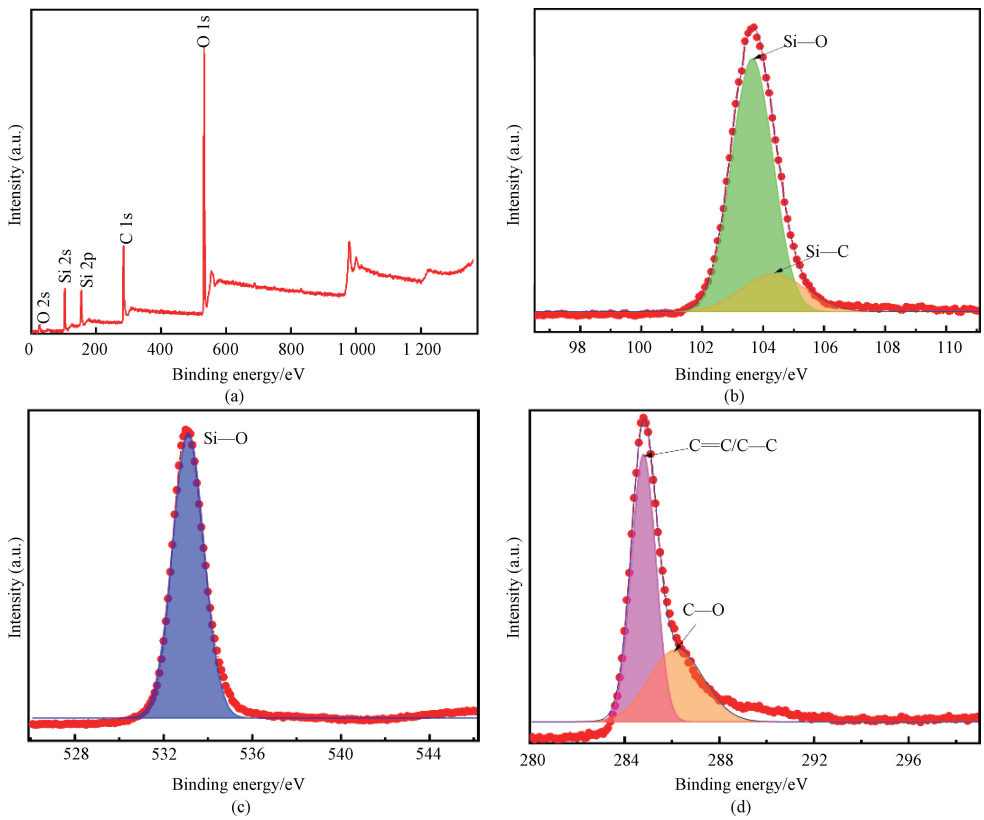

Fig. 6 XPS spectra: (a) necklace-like CNTs@SiOC; (b) Si 2p; (c) O 1s; (d) C 1s

2.3 Electrochemical performance

CV curves of the necklace-like CNTs@SiOC electrode at a scan rate of 0.1 mV/s are shown in Fig. 7(a). A sharp cathodic peak emerges at 0 V (vs. Li^+/Li) and a weak anodic peak at 0.71 V can be observed for the necklace-like CNTs @ SiOC electrode, which is similar to that reported in Ref. [38]. The Li-storage mechanism of the necklace-like CNTs @ SiOC electrode is not clear.

However, it might be similar to that of hard carbon anodes as reported in Ref. [39]. Figure 7(b) shows the rate performance of CNTs @ SiOC-5 and CNTs @ SiOC-15 electrodes. The prepared electrodes are cycled at a current density of 100–2 000 mA/g, and the rate performance decreases progressively due to the formation of solid electrolyte interface (SEI). When the current density returns to 100 mA/g, the specific capacity improves.

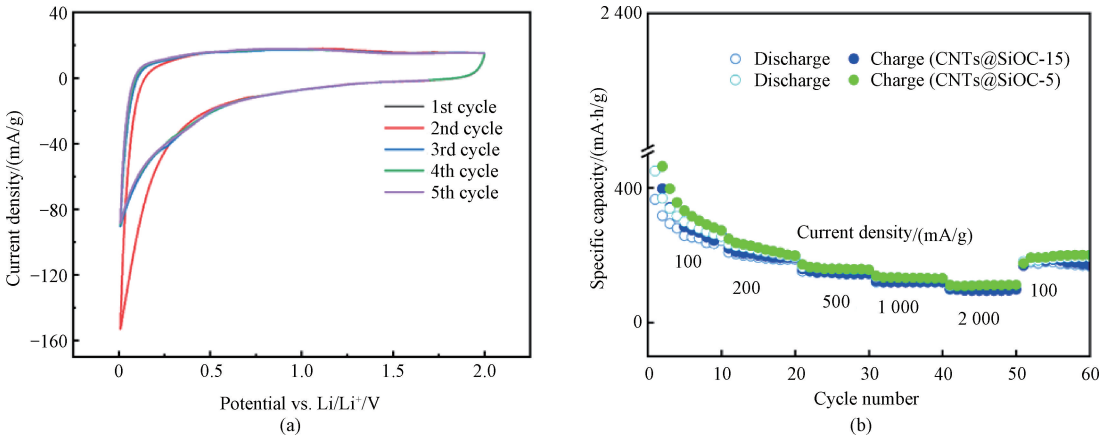

Fig. 7 Electrochemical performance: (a) CV curves of necklace-like CNTs@SiOC electrode for the first five cycles at a scan rate of 0.1 mV/s; (b) rate performance of CNTs@SiOC-5 and CNTs@SiOC-15 electrodes

The GCD cycling ability was assessed within the voltage range of 0.01 to 2.00 V (vs. Li/Li^+), and the first discharging/charging curves were performed at 100 mA/g. The necklace-like CNTs @ SiOC electrode provide the initial discharging and charging specific capacities as 1 413 and 458 mA·h/g (Fig. 8(a)). In contrast, SiOC, CNTs @ SiOC-5 and CNTs @ SiOC-15 provide the initial discharging specific capacities of 1 638, 1 450, and 1 621 mA·h/g and the initial charging specific capacities of 479, 469, and 317 mA·h/g, respectively. Such irreversible loss of the initial specific capacity is caused by the SEI formation layer. Therefore, the initial coulombic efficiencies are lower for the first discharging/charging cycle. During the first discharging/charging cycle, an SEI layer forms on the surface of the SiOC-based electrode. This SEI layer consumes some Li ions during formation of cells, leading to a lower initial charging specific capacity. This consumption of Li ions during formation is the main reason for higher initial discharging specific capacity. As a result, every electrode material's initial discharging specific capacity is higher than its initial charging specific capacity. Previous studies have reported similar outcomes regarding the irreversible loss of the initial specific capacity during the first discharging/charging cycle[12, 22, 40]. The initial coulombic efficiencies of SiOC, CNTs @ SiOC-5, CNTs @ SiOC-15, and necklace-like CNTs@SiOC are 29.24%, 32.00%, 19.55%, and 32.00%, respectively.

Furthermore, the necklace-like CNTs@SiOC electrode also exhibits superior stability of 263 mA·h/g at a current density of 100 mA/g up to 200 cycles (Fig. 8(b)). The necklace-like CNTs @ SiOC electrode shows better rate performance compared to the SiOC electrode by delivering reversible specific capacities of 383.18, 256.35, 179.46, 137.97, and 89.72 mA·h/g at current densities of 100, 200, 500, 1 000 and 2 000 mA/g, respectively (Fig. 8(c)). Once the current density recovers to its initial value of 100 mA/g, the specific capacity of the necklace-like CNTs@SiOC electrode is restored to 220 mA·h/g. In contrast, the SiOC electrode exhibits inferior specific capacities and rate performance. Besides, CNTs @ SiOC-5 and CNTs @ SiOC-15 electrodes also exhibit better rate performance than the SiOC anode but lower than the necklace-like CNTs@SiOC electrode. When the current density returns to 100 mA/g, the specific capacity improves as reported in Ref. [41]. The improved rate performance of the necklace-like CNTs@SiOC electrode is due to its interconnected conductive pathways and nanochannels of Li-ion diffusion.

The long cycling performance of necklace-like CNTs@SiOC and SiOC electrodes was evaluated at 500 mA/g. SiOC, CNTs @ SiOC-5, and CNTs @ SiOC-15 electrodes provide a specific capacity of 117, 115 and 137 mA·h/g after 1 000 cycles at a current density of 500 mA/g. Whereas, the necklace-like CNTs @ SiOC electrode exhibits superior stability with a specific capacity of 178 mA·h/g after 1 400 discharging/charging cycles at a current density of 500 mA/g (Fig. 8(d)). The long cycling performance of the necklace-like CNTs@SiOC electrode could be attributed to CNTs that provide a stable conductive network, ensure full utilization of active sites and alleviate the mechanical stress generated during discharging/charging. The necklace-like CNTs @ SiOC demonstrates significantly improved stability, maintaining performance up to 1 400 cycles, surpassing that of other SiOC-based structures. For comparison, the SiOC-CNT composite is stable up to 40 cycles[20], Hp-SiOC@VG is stable up to 600 cycles[17], S-DVB-1 is stable up to 500 cycles[7], SiOC@C/rGO is stable up to 200 cycles[11], and Si—O—C composite is stable up to 40 cycles[42].

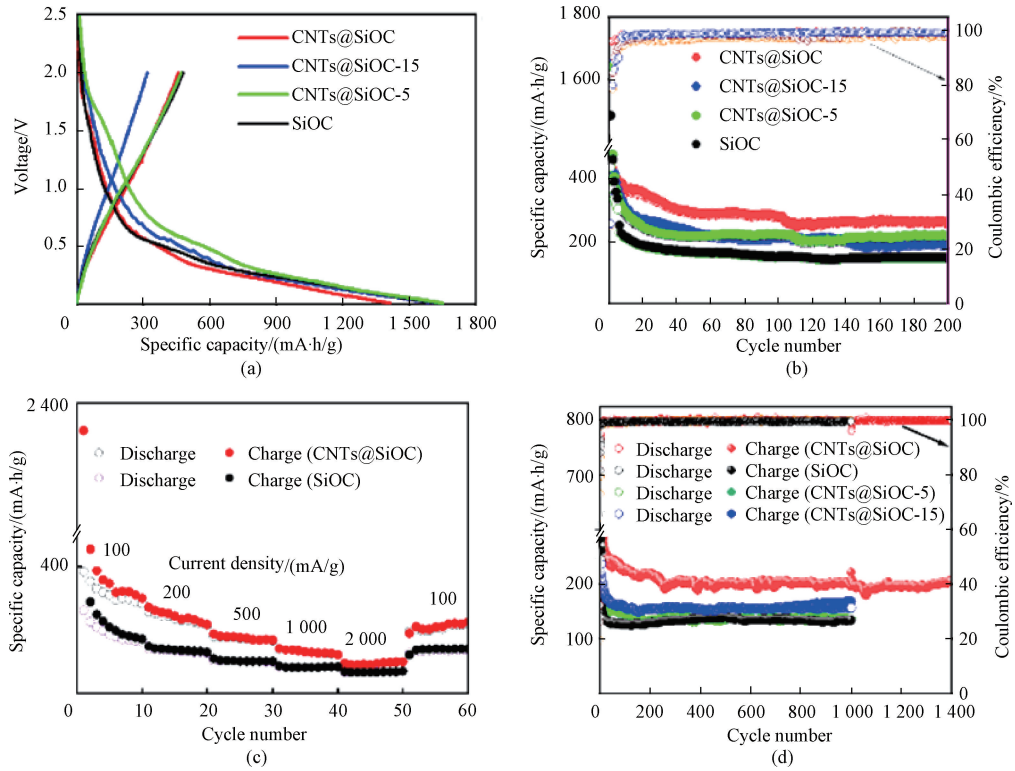

Fig. 8 Electrochemical performance of SiOC, CNTs @ SiOC-5, CNTs @ SiOC-15 and necklace-like CNTs @ SiOC electrodes: (a) the first discharging/charging curves; (b) cycling performance at 100 mA/g; (c) rate performance; (d) long cycling performance at 500 mA/g

The special structural characteristics of the necklace-like CNTs@SiOC electrode are responsible for its better electrochemical performance. The structural integrity of SiOC and necklace-like CNTs@SiOC electrodes was further investigated by FESEM (Fig. 9). The SiOC electrode suffers from severe surface cracking after 1 000 cycles due to structural deterioration. To further demonstrate the long-term structural stability of CNTs @ SiOC, the electrode surface morphological change was characterized before and after 1 400 cycles. The necklace-like CNTs @ SiOC electrode retains its integrity after 1 400 cycles, and only the surface roughening is observed with no crack formation because the porous structure resembling a necklace allows for volume expansion (Fig. 9(d)).

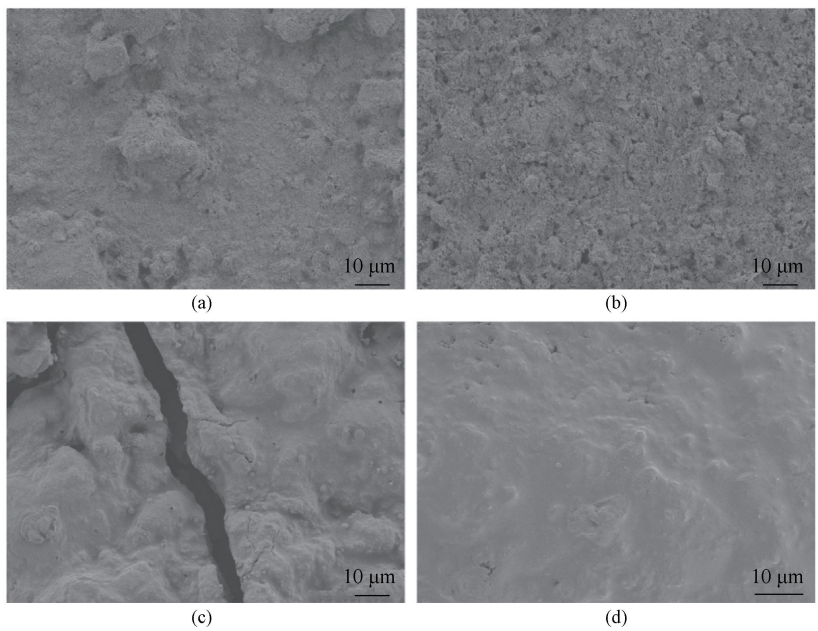

Fig. 9 FESEM images: (a) SiOC electrode before cycling; (b) SiOC electrode after 1 000 cycles; (c) necklace-like CNTs@SiOC electrode before cycling; (d) necklace-like CNTs@SiOC electrode after 1 400 cycles

3 Conclusions

In this study, we have demonstrated a new method to fabricate a necklace-like CNTs@SiOC electrode for LIBs by incorporating SiOC around CNTs. The novel necklace-like CNTs@SiOC exhibited better electrochemical performance than SiOC, CNTs@SiOC-5, and CNTs@SiOC-15. The necklace-like CNTs@SiOC provided a stable specific capacity of 178 mA·h/g after 1 400 discharging/charging cycles at a current density of 500 mA/g. CNTs play a key role in maintaining a stable conductive pathway during discharging/charging within necklace-like CNTs@SiOC.

References

[1] DIOUF B, PODE R. Potential of lithium-ion batteries in renewable energy[J]. *Renewable Energy*, 2015, 76: 375-380.

[2] TOKI G F I, HOSSAIN M K, REHMAN W U, et al. Recent progress and challenges in silicon-based anode materials for lithium-ion batteries[J]. *Industrial Chemistry & Materials*, 2024, 2(2): 226-269.

[3] JIANG M M, CHEN J L, LUO H X, et al. Building interconnected structures with silicon-based nanospheres and TiN ionic fence enables ultrahigh electrochemical stability[J]. *Advanced Functional Materials*, 2024, 34(27): 2316568.

[4] SEOK E, CHOI M, PARK D, et al. Synthesis of size-controlled SiOC ceramic materials by silicone oil-based emulsion method for anodes in lithium-ion batteries[J]. *Journal of Alloys and Compounds*, 2023, 969: 172386.

[5] RAHMAN M A, SONG G S, BHATT A I, et al. Nanostructured silicon anodes for high-performance lithium-ion batteries[J]. *Advanced Functional Materials*, 2016, 26(5): 647-678.

[6] KU M, PARK D, KIM M, et al. Hydrophobic dispersion-derived Si/rGO nanocomposites in SiOC ceramic matrix as anode materials for high performance lithium-ion batteries[J]. *Journal of Materials Chemistry A*, 2023, 11(28): 15277-15285.

[7] WU P F, GUO X X, SU Z M, et al. Preparation of silicon oxycarbide (SiOC) anodes for high performance Li-ion batteries using competitive relationship between crosslinking and polymerization[J]. *Chemical Engineering Journal*, 2022, 446: 137354.

[8] SUJITH R, GANGADHAR J, GREENOUGH M, et al. A review of silicon oxycarbide ceramics as next generation anode materials for lithium-ion batteries and other electrochemical applications[J]. *Journal of Materials Chemistry A*, 2023, 11(38): 20324-20348.

[9] HAN Q, ZHANG J Z, CHEN H X, et al. The effect of graphitization degree of carbon and Si—O—C network on the electrochemical performance of SiOC anodes[J]. *International Journal of Applied Ceramic Technology*, 2024, 21(3): 2332-2341.

[10] BIN MUJIB S, RASHEED M, SINGH G. Evaluating use of boron- and hafnium-modified polysilazanes for ceramic matrix minicomposites[J]. *ACS Omega*, 2022, 7(49): 45325-45335.

[11] MA M B, WANG H J, XIONG L, et al. Self-assembled homogeneous SiOC@C/graphene with three-dimensional lamellar structure enabling improved capacity and rate performances for lithium ion storage[J]. *Carbon*, 2022, 186: 273-281.

[12] PRADEEP V S, AYANA D G, GRACZYK-ZAJAC M, et al. High rate capability of SiOC ceramic aerogels with tailored porosity as anode materials for Li-ion batteries[J]. *Electrochimica Acta*, 2015, 157: 41-45.

[13] FAN S Z, ZHANG J J, CUI S Q, et al. Large-scale synthesis of SiOC composites for stable Li-ion battery anode and dendrite-free Li metal deposition[J]. *Chemical Engineering Journal*, 2024, 479: 147785.

[14] LEE S H, PARK C, DO K, et al. Maximizing the utilization of active sites through the formation of native nanovoids of silicon oxycarbide as anode materials in lithium-ion batteries[J]. *Energy Storage Materials*, 2021, 35: 130-141.

[15] ZHU G J, GUO R, LUO W, et al. Boron doping-induced interconnected assembly approach for mesoporous silicon oxycarbide structure[J]. *National Science Review*, 2021, 8(6): nwaa152.

[16] PARK J, KIM M, CHOI M, et al. Sb/C composite embedded in SiOC buffer matrix via dispersion property control for novel anode material in sodium-ion batteries[J]. *Journal of Power Sources*, 2023, 568: 232908.

[17] LI K Z, YUAN G Q, LIU X F, et al. On the practical applicability of rambutan-like SiOC anode with enhanced reaction kinetics for lithium-ion storage[J]. *Advanced Functional Materials*, 2023, 33(43): 2302348.

[18] XIA K D, LIU X, LIU H, et al. Carbon-enriched SiOC ceramics with hierarchical porous structure as anodes for lithium storage[J]. *Electrochimica Acta*, 2021, 372: 137899.

[19] FENG X M, CHEN H X, ZHANG J Z, et al. Constructing a conductive nest to improve the electrochemical properties of SiOC anodes through CNT additives[J]. *Journal of Electronic Materials*, 2024, 53(2): 1074-1082.

[20] BHANDAVAT R, SINGH G. Stable and efficient Li-ion battery anodes prepared from polymer-derived silicon oxycarbide-carbon

nanotube shell/core composites[J]. *The Journal of Physical Chemistry C*, 2013, 117: 11899-1190.
[21] WU Z, CHENG X Q, TIAN D, et al. SiOC nanolayers directly-embedded in graphite as stable anode for high-rate lithium ion batteries[J]. *Chemical Engineering Journal*, 2019, 375: 121997.
[22] LIU W M, JIANG M M, ZHANG F Z, et al. Confined self-assembly of SiOC nanospheres in graphene film to achieve cycle stability of lithium ion batteries[J]. *New Journal of Chemistry*, 2022, 46(14): 6519-6527.
[23] SHAO G F, HANAOR D A H, WANG J, et al. Polymer-derived SiOC integrated with a graphene aerogel as a highly stable Li-ion battery anode[J]. *ACS Applied Materials & Interfaces*, 2020, 12(41): 46045-46056.
[24] ZHANG Y Y, YANG W, LIU X, et al. Necklace-structured silicon suboxide-based anode materials with multiple carbon networks for stable lithium storage[J]. *Advanced Functional Materials*, 2024, 34(25): 2315680.
[25] YANG H, NEAL L, FLORES E E, et al. Role and impact of surfactants in carbon nanotube dispersions and sorting[J]. *Journal of Surfactants and Detergents*, 2023, 26(5): 607-622.
[26] RICHARD C, BALAVOINE F, SCHULTZ P, et al. Supramolecular self-assembly of lipid derivatives on carbon nanotubes[J]. *Science*, 2003, 300(5620): 775-778.
[27] HUANG Y B, YUAN P, WU Z W, et al. Preparation of surface-silylated and benzene-bridged Ti-containing mesoporous silica for cyclohexene epoxidation[J]. *Journal of Porous Materials*, 2016, 23(4): 895-903.
[28] ISLAM M F, ROJAS E, BERGEY D M, et al. High weight fraction surfactant solubilization of single-wall carbon nanotubes in water[J]. *Nano Letters*, 2003, 3(2): 269-273.
[29] MANNE S, CLEVELAND J P, GAUB H E, et al. Direct visualization of surfactant hemimicelles by force microscopy of the electrical double layer[J]. *Langmuir*, 1994, 10(12): 4409-4413.
[30] BAO Y, WANG T, KANG Q L, et al. Micelle-template synthesis of hollow silica spheres for improving water vapor permeability of waterborne polyurethane membrane[J]. *Scientific Reports*, 2017, 7: 46638.
[31] ZHANG M, WU Y P, FENG X Z, et al. Fabrication of mesoporous silica-coated CNTs and application in size-selective protein separation[J]. *Journal of Materials Chemistry*, 2010, 20(28): 5835-5842.
[32] PENG Y Q, WANG K S, YU M H, et al. An optimized process for in situ formation of multi-walled carbon nanotubes in templated pores of polymer-derived silicon oxycarbide[J]. *Ceramics International*, 2017, 43(4): 3854-3860.
[33] HALIM M, HUDAYA C, KIM A Y, et al. Phenyl-rich silicone oil as a precursor for SiOC anode materials for long-cycle and high-rate lithium ion batteries[J]. *Journal of Materials Chemistry A*, 2016, 4(7): 2651-2656.
[34] LU K, LI J K. Fundamental understanding of water vapor effect on SiOC evolution during pyrolysis[J]. *Journal of the European Ceramic Society*, 2016, 36(3): 411-422.
[35] ERMAKOVA M A, ERMAKOV D Y, PLYASOVA L M, et al. XRD studies of evolution of catalytic nickel nanoparticles during synthesis of filamentous carbon from methane[J]. *Catalysis Letters*, 1999, 62(2): 93-97.
[36] SORARÙ G D, D'ANDREA G, GLISENTI A. XPS characterization of gel-derived silicon oxycarbide glasses[J]. *Materials Letters*, 1996, 27(1/2): 1-5.
[37] VASHISTH A, KHATRI S, HAHN S H, et al. Mechanical size effects of amorphous polymer-derived ceramics at the nanoscale: experiments and ReaxFF simulations[J]. *Nanoscale*, 2019, 11(15): 7447-7456.
[38] SHI H M, YUAN A B, XU J Q. Tailored synthesis of monodispersed nano/submicron porous silicon oxycarbide (SiOC) spheres with improved Li-storage performance as an anode material for Li-ion batteries[J]. *Journal of Power Sources*, 2017, 364: 288-298.
[39] FUKUI H, OHSUKA H, HINO T, et al. A Si—O—C composite anode: high capability and proposed mechanism of lithium storage associated with microstructural characteristics[J]. *ACS Applied Materials & Interfaces*, 2010, 2(4): 998-1008.
[40] ZHU G J, JIANG M M, MA Y Y, et al. A carbon network strategy to synthesize silicon-carbon anodes toward regulated morphologies during molten salt reduction[J]. *CrystEngComm*, 2020, 22(29): 4894-4902.
[41] DAVID L, BHANDAVAT R, BARRERA U, et al. Silicon oxycarbide glass-graphene composite paper electrode for long-cycle lithium-ion batteries[J]. *Nature Communications*, 2016, 7: 10998.
[42] LIU X, ZHENG M C, XIE K. Mechanism of lithium storage in Si—O—C composite anodes[J]. *Journal of Power Sources*, 2011, 196(24): 10667-10672.

项链状 CNTs@SiOC 纳米结构材料实现稳定锂离子存储

GAZI Farhan Ishraque Toki, RANA Zafar Abbas Manj, 马元元*, 杨建平*
东华大学 先进纤维材料全国重点实验室 材料科学与工程学院, 上海 201620

摘　要: 硅氧碳化物（silicon oxycarbide, SiOC）凭借其独特的性质已成为锂离子电池（Li-ion battery, LIB）负极材料的理想材料之一。然而, SiOC 的低导电率限制了其实际应用。本文通过溶胶-凝胶法制备了一种新颖的项链状纳米结构: 通过在 SiOC 纳米颗粒中嵌入碳纳米管（carbon nanotube, CNT）, 在其内部形成了稳定的电子通道。通过在煅烧前去除十六烷基三甲基溴化铵（hexadecyl trimethyl ammonium bromide, CTAB）和离心分离 SiOC 与 CNTs@PBMO 颗粒来控制 CTAB 含量是实现项链状 CNTs@SiOC 纳米结构材料的关键。所制备的多孔项链状 CNTs@SiOC 纳米结构不仅提高了导电率, 而且在充放电过程中实现了 SiOC 活性位点的充分利用, 并加速了离子的迁移。因此, 经过 1 400 个循环后, CNTs@SiOC 纳米结构材料的容量仍能保持 178 mA·h/g。

关键词: 项链状结构; CNTs@SiOC; 溶胶-凝胶法; 长循环; 锂离子电池